Atmos. Chem. Phys., 14, 1055–1073, 2014
www.atmos-chem-phys.net/14/1055/2014/
doi:10.5194/acp-14-1055-2014

Atmospheric Chemistry and Physics Open Access

Nitric acid trihydrate nucleation and denitrification in the Arctic stratosphere

J.-U. Grooß[1], I. Engel[1,2], S. Borrmann[3,4], W. Frey[4,*], G. Günther[1], C. R. Hoyle[2,5], R. Kivi[6], B. P. Luo[2], S. Molleker[3], T. Peter[2], M. C. Pitts[7], H. Schlager[8], G. Stiller[9], H. Vömel[10], K. A. Walker[11], and R. Müller[1]

[1]Institut für Energie- und Klimaforschung – Stratosphäre (IEK-7), Forschungszentrum Jülich, Germany
[2]Institute for Atmospheric and Climate Science, ETH Zurich, Zurich, Switzerland
[3]Institut für Physik der Atmosphäre, Johannes-Gutenberg-Universität Mainz, Germany
[4]Abteilung Partikelchemie, Max Planck Institut für Chemie, Mainz, Germany
[5]Paul Scherrer Institute, Villigen, Switzerland
[6]Finnish Meteorological Institute, Sodankylä, Finnland
[7]NASA Langley Research Center, Hampton, VA, USA
[8]Institut für Physik der Atmosphäre, Deutsches Zentrum für Luft- und Raumfahrt, Oberpfaffenhofen, Germany
[9]Institute for Meteorology and Climate Research, Karlsruhe Institute of Technology, Karlsruhe, Germany
[10]Meteorological Observatory Lindenberg, Deutscher Wetterdienst, Germany
[11]Department of Physics, University of Toronto, Ontario, Canada
[*]now at: School of Earth Sciences, The University of Melbourne, Melbourne, Australia

Correspondence to: J.-U. Grooß (j.-u.grooss@fz-juelich.de)

Received: 8 August 2013 – Published in Atmos. Chem. Phys. Discuss.: 23 August 2013
Revised: 17 December 2013 – Accepted: 20 December 2013 – Published: 29 January 2014

Abstract. Nitric acid trihydrate (NAT) particles in the polar stratosphere have been shown to be responsible for vertical redistribution of reactive nitrogen (NO_y). Recent observations by Cloud–Aerosol Lidar with Orthogonal Polarization (CALIOP) aboard the CALIPSO satellite have been explained in terms of heterogeneous nucleation of NAT on foreign nuclei, revealing this to be an important formation pathway for the NAT particles. In state of the art global- or regional-scale models, heterogeneous NAT nucleation is currently simulated in a very coarse manner using a constant, saturation-independent nucleation rate. Here we present first simulations for the Arctic winter 2009/2010 applying a new saturation-dependent parametrisation of heterogeneous NAT nucleation rates within the Chemical Lagrangian Model of the Stratosphere (CLaMS). The simulation shows good agreement of chemical trace species with in situ and remote sensing observations. The simulated polar stratospheric cloud (PSC) optical properties agree much better with CALIOP observations than those simulated with a constant nucleation rate model. A comparison of the simulated particle size distributions with observations made using the Forward Scattering Spectrometer Probe (FSSP) aboard the high altitude research aircraft Geophysica, shows that the model reproduces the observed size distribution, except for the very largest particles above 15 µm diameter. The vertical NO_y redistribution caused by the sedimentation of the NAT particles, in particular the denitrification and nitrification signals observed by the ACE-FTS satellite instrument and the in situ SIOUX instrument aboard the Geophysica, are reproduced by the improved model, and a small improvement with respect to the constant nucleation rate model is found.

1 Introduction

It has been known for more than a decade that large nitric acid containing particles of over 10 µm diameter can be present in the cold polar stratosphere (Fahey et al., 2001). These particles are thought to be responsible for the vertical redistribution of NO_y in the stratosphere, namely denitrification above altitudes of about 18 km and nitrification below. The process of denitrification is important for ozone

depletion as it reduces springtime HNO_3 and thus slows down the chlorine deactivation which occurs through the reaction $ClO + NO_2$ at the end of the polar winter (e.g. Müller et al., 1994). Simulations using Lagrangian particle tracking have shown that it is possible to explain the observed denitrification by the vertical HNO_3 transport caused by the sedimentation of these large particles, which are assumed to consist of nitric acid trihydrate (NAT) (Carslaw et al., 2002; Grooß et al., 2005). For the Lagrangian particle trajectories in the latter two studies a constant, air-volume based NAT nucleation rate was applied (i.e. constant number of nucleations per time unit per volume of air) whenever temperatures were below the NAT existence temperature T_{NAT}. Besides this on/off dependence for $T < T_{NAT}$ or $T > T_{NAT}$ no other temperature dependence was taken into account because of lacking experimental or observational information (Carslaw et al., 2002; Grooß et al., 2005). For the winter 2002/2003, a simulation with the nucleation rate derived from a single observation, where the NAT nucleation rate in the absence of ice could be constrained (Voigt et al., 2005), reproduced the basic features of the observed denitrification and nitrification (Grooß et al., 2005). However, for other Arctic winters a nucleation rate with a three times lower value needed to be chosen to successfully simulate the observed denitrification (Davies et al., 2005).

Recently, studies based on CALIOP data confirmed previous speculations, that heterogeneous nucleation on foreign particles, probably of meteoritic origin, contributes to the NAT nucleation in the polar stratosphere (Hoyle et al., 2013; Engel et al., 2013). Using microphysical model calculations of the Zurich Optical and Microphysical box Model (ZOMM) along back-trajectories, the saturation-dependence of NAT particle nucleation could be determined (Hoyle et al., 2013). This information is used here to construct a new NAT nucleation parametrisation for the Chemical Lagrangian Model of the Stratosphere (CLaMS).

To this end, we present a comparison between CLaMS simulations and observations for the Arctic winter 2009/2010, in which the extensive measurement campaign of the project RECONCILE (von Hobe et al., 2013) provided detailed measurements. The aim of this work is to constrain the value of the NAT nucleation rate by means of polar stratospheric clouds (PSC) observations, especially those by the Cloud–Aerosol Lidar with Orthogonal Polarization (CALIOP) aboard the CALIPSO satellite (Pitts et al., 2009) and in this way improve the simulated denitrification.

Even though the vortex in winter 2009/2010 experienced a vortex split event in early December and was one of the warmest winters within the last two decades, when averaging December–March, the period between mid-December 2009 and end of January 2010 was exceptionally cold (Dörnbrack et al., 2012). During this period, space-borne Lidar observations by CALIOP indicated more PSCs than in previous Arctic seasons, with significantly more observations of ice clouds and higher number densities of NAT particles than hitherto observed by CALIOP (Pitts et al., 2011).

In addition to the present study, CLaMS has been used in a very similar configuration, however with a constant NAT nucleation rate, in several other recent works examining the Arctic winter of 2009/2010. For example, Hösen (2013) investigated in situ tracer observations, while Woiwode (2013) and Kalicinsky et al. (2013) used CLaMS to interpret the remote sensing observations of the aircraft instruments MIPAS-ENVISAT and CRISTA-NF, respectively. Further, Wohltmann et al. (2013) performed simulations with a focus on the sensitivity of polar chlorine chemistry and ozone loss on heterogeneous reactions, also using a constant NAT nucleation rate. Wohltmann et al. (2013) concluded that changes in the underlying assumptions on chlorine activation have only a small impact on the modelled ozone loss. This result confirms the finding by Wegner et al. (2012) and Drdla and Müller (2012) that substantial chlorine activation occurs on cold binary aerosols. However, uncertainties in NAT microphysics contribute most to the overall uncertainty in modelling heterogeneous chemistry and even though an increase in surface area due to NAT particles is of minor importance for modelling heterogeneous chemistry, the removal of reactive nitrogen due to denitrification remains important as it slows down chlorine deactivation.

2 Model description

2.1 CLaMS

The Chemical Lagrangian Model of the Stratosphere (CLaMS) is a Chemistry Transport Model that is based upon the Lagrangian principle (McKenna et al., 2002a, b; Konopka et al., 2004). The chemical composition of the atmosphere is simulated for multiple air parcels that represent the gas-phase compositions of the air volumes centred at the individual trajectory locations and that are moving due to advection. Interaction between the air parcels is realised by an anisotropic mixing scheme (McKenna et al., 2002a; Konopka et al., 2005). The model also includes the Lagrangian simulation of NAT particles which are traced individually by so-called particle parcels. Each particle parcel is assigned a number density upon nucleation and it represents this particle density over the average volume of an air parcel. Growth, evaporation and gravitational settling are simulated along their individual trajectories (Grooß et al., 2005). Due to the sedimentation of the NAT particles, the particle parcels are not congruent with the air parcels. Hemispheric simulations starting on 1 December 2009 were carried out using CLaMS with two different spatial resolutions. The standard high resolution simulation (HR) has a horizontal resolution of 70 km northward of 10° N and 100 km between 0 and 10° N. The vertical model range is between 320 and 900 K, divided into 50 levels, resulting in a vertical resolution of about 450–500 m

between 20 and 25 km altitude. This simulation uses about 2.9 million air parcels. Besides this simulation, a lower resolution hemispheric configuration was used, with a horizontal resolution of 100 km northward of 40° N, and 300 km southward of 40° N, comparable to earlier simulations, (e.g. Grooß and Müller, 2007). This configuration uses about 380 000 air parcels in 32 vertical levels and a vertical resolution of about 700 m between 20 and 25 km altitude. It was used for various sensitivity simulations, as described below. Also some evaluations that require large data output were based on the lower resolution configuration.

The underlying wind and temperature fields are taken from the ERA-Interim analysis data provided by the European Centre of Medium-Range Weather Forecasts (ECMWF) (Dee et al., 2011). The CLaMS simulations use a hybrid vertical coordinate ζ, that is equal to potential temperature above about 300 hPa and transitions to a pressure-like coordinate below this pressure (Konopka et al., 2007; Riese et al., 2012). As most of the analysis of this study refers to altitudes above the 300 hPa level, the vertical coordinate ζ can be interpreted here as potential temperature. The vertical velocities are derived from ERA-Interim total diabatic heating rates (Ploeger et al., 2010). For the CLaMS mixing parametrisation that is described elsewhere (McKenna et al., 2002a; Konopka et al., 2005), a time step of 24 h and a critical Lyapunov coefficient (that is basically the critical wind shear above which the CLaMS mixing algorithm is triggered) of 1.5 day^{-1} were used similar as in the study by Riese et al. (2012).

As microphysical properties of PSCs are highly temperature dependent, it is very important to base the simulations on realistic temperature data. Engel et al. (2013) indicated that the ERA-Interim temperature data compared better with the radiosonde observations than other available meteorological analyses. Temperature fluctuations occurring on timescales below the 6 h resolution of the ERA-Interim data used here were shown to have a relatively small impact on the NAT nucleation rates (Hoyle et al., 2013). Further, the effects of such unresolved temperature changes in the model meteorological fields are implicitly accounted for in the NAT nucleation parametrisation.

The CLaMS simulations include dynamical tracers such as passive ozone and passive NO_y, that are not influenced by chemistry. These were initialised at the beginning of the simulations with the ozone and NO_y fields, respectively. The difference between these tracers and their chemically active counterparts can be used to quantify changes due to chemistry or particle sedimentation.

Stratospheric chemistry in CLaMS is an updated version of the scheme described in McKenna et al. (2002b). It now comprises 143 reactions of 45 variable chemical species, now explicitly containing reactions of importance in the upper stratosphere (e.g. reactions involving H radicals as well as N_2O and CFCs). The detailed list of reactions included in CLaMS is given in Table A1 in the appendix. Chemical reaction rates and absorption cross sections are based on Sander et al. (2011) including ClOOCl photolysis, which is based on Papanastasiou et al. (2009). Exceptions are the reaction rate for ClOOCl formation, which is taken from Nickolaisen et al. (1994) and the ClOOCl equilibrium constant which is taken from Plenge et al. (2005). These values are based on Geophysica measurements as suggested by Sumińska-Ebersoldt et al. (2012). Heterogeneous reaction rates on liquid aerosol particles are based on the parametrisation of Shi et al. (2001), see also Wegner et al. (2012) for details. As the NAT particles are handled in a separate sedimentation module at locations not congruent with the air parcels, the heterogeneous reactions on the NAT particles could not be considered here, which is justified since the liquid particles in the polar stratosphere are mostly responsible for the heterogeneous reactions leading to the activation of the halogens (Solomon, 1999; Drdla and Müller, 2012; Wegner et al., 2012).

The Lagrangian sedimentation scheme described by Grooß et al. (2005) was used to simulate the vertical redistribution of NO_y. However, the nucleation rate of NAT particles was adapted to the new parametrisation as described below. Within this scheme, the advection of the NAT particles is calculated in a Lagrangian way along individual trajectories. Each particle parcel represents a number of particles with identical characteristics distributed over a volume equal to the size of one air parcel. To this end, a number concentration is assigned to each particle parcel that is assumed to be constant over the particular volume. Within the volume of one air parcel, multiple particle parcels with different characteristics are common describing the particle size distribution. The locations for possible NAT nucleation per day were homogeneously distributed in space with a 4 times higher density than that of the air parcels. For a test if this ratio between daily nucleating NAT particle parcels and air parcels is sufficient, the ratio was increased in a sensitivity study from 4 to 64 with a decreasing corresponding assigned number density. Growth and evaporation of the individual particles was calculated depending on temperature and gas-phase HNO_3 and H_2O of the neighbouring air parcels. Vertical descent due to sedimentation of the particles is included. The NAT particles are assumed to have the shape of compact spheres.

The dehydration of the air masses that typically occurs at the tropopause level is implemented using a temperature-dependent parametrisation for heterogeneous ice freezing (Krämer et al., 2009). Water ice is irreversibly removed if the inferred particle fall speed exceeds a prescribed threshold value (von Hobe et al., 2011). This parametrisation also allows for dehydration in the stratosphere to be simulated that was observed during January 2010 (Khaykin et al., 2013).

The chemical initialisation of the simulation for 1 December 2009, 12:00 UTC, was based on satellite data, on MIPAS-ENVISAT (updated version 5 data from von Clarmann et al., 2009) and ACE-FTS (version 3.0) (Bernath et al., 2005), and observed tracer correlations. Additionally, we used data from a multi-annual CLaMS simulation with simplified chemistry

(Pommrich et al., 2011; Ploeger et al., 2013). The details for the individual species are given below.

N_2O was initialised from the multi-annual CLaMS simulation below 400 K and from MIPAS-ENVISAT above 500 K with a linear transition in between. O_3 was initialised above 400 K from MIPAS-ENVISAT data within ±2 days. The observation locations were transformed to the synoptic initialisation time using CLaMS trajectories and gridded to a 2° × 6° grid. Below 350 K, O_3 was taken from the multi-annual simulation with a linear transition in between. Similarly, H_2O was gridded from MIPAS-ENVISAT data above 600 K and taken from the CLaMS multi-annual simulation below 350 K with a linear transition in between. The initialisation of CH_4 was derived from N_2O using the correlation from ACE-FTS N_2O and CH_4 data from November 2009 for equivalent latitudes > 65° N. Cl_y and Br_y were derived from CH_4 data correlation after Grooß et al. (2002), where Br_y is increased by 10 % to account for the increase in bromine-containing source gases since the year 2000. Total inorganic nitrogen NO_y could also be initialised from a correlation with N_2O from ACE-FTS data, since ACE-FTS observed all major compounds of NO_y (Jones et al., 2011). For the species CO, CFC-12, CH_3Cl, CFC-22, CCl_4, and CFC-113 a correlation was also derived from ACE-FTS version 3.0 data in November 2009. HNO_3 was derived similarly to O_3 from gridded MIPAS-ENVISAT data, whereas the remaining NO_y species were scaled linearly to fit the derived total sum of NO_y. CFC-11 mixing ratios were derived from N_2O using data correlation from ACE-FTS version 3.0 for November 2009 and different equivalent latitude ranges (10° S–10° N , 20° N–40° N, 40° N–60° N, and > 60° N). The polynomial fits of all these correlations are listed in Table A2 in the appendix. The remaining minor species as well as the partitioning within the various chemical families are taken from the Mainz 2-D model (Grooß, 1996). The sulfate aerosol vertical distribution was initialised consistent with an aerosol surface area density climatology for the months November and December 1998/99, a period with low aerosol particle content (similar to the conditions for the 2009/2010 Arctic winter) from a climatology compiled by D. Considine (Eyring et al., 2006), that is based on SAGE II data for these years.

The boundary conditions at the upper boundary at 900 K were derived from observations similar to the initialisation for two times per month. The mixing ratios of N_2O, H_2O, and HNO_3 were taken from MIPAS-ENVISAT and averaged to equivalent latitude bins. At the lower boundary of the simulations in the free troposphere ($\zeta = 320$ K, corresponding to $\theta = 320$ K within ±5 K at polar latitudes), no modification was made such that the chemical composition and the lower boundary is determined only from the initialisation and transport, predominantly the vertical descent inside the polar vortex.

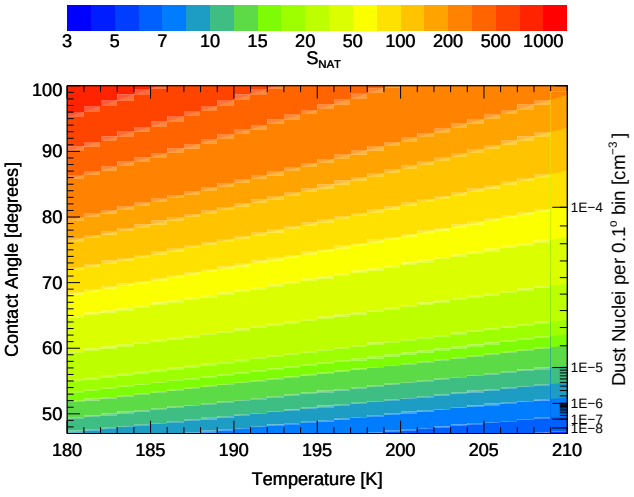

Fig. 1. Supersaturation needed for NAT nucleation for each 0.1° wide contact angle bin displayed as function of contact angle and temperature derived from Hoyle et al. (2013). The second vertical axis shows the corresponding number of dust particles per bin.

2.2 Parametrisation of NAT nucleation

Hoyle et al. (2013) demonstrate that heterogeneous nucleation is needed to explain the occurrence of NAT PSCs observed in the Arctic during the second half of December 2009. A potential source of heterogeneous nuclei is meteoritic dust immersed in stratospheric aerosol particles (Curtius et al., 2005). Hoyle et al. (2013) showed that a constant nucleation rate cannot explain the observed CALIOP PSC data. They assumed that heterogeneous nucleation is triggered by active sites of the individual dust particles and that the nucleation efficiency of these active sites can be characterised by a distribution of contact angles. The occurrence probability distribution of the contact angles is shown in Fig. 2 of Hoyle et al. (2013). For the implementation of the heterogeneous NAT nucleation rates into CLaMS, some modifications needed to be made. While in the study of Hoyle et al. (2013), the ZOMM simulations were performed on 10-day back-trajectories that exclusively started at temperatures above T_{NAT}, the nucleation in a chemical transport model must be handled differently. Here we use the 24 h forward air mass trajectories of the CLaMS simulation of which some may start at temperatures below T_{NAT}. The supersaturations required to nucleate a NAT particle in a specific contact angle bin within a 1 h time interval were derived from the parametrisation of Hoyle et al. (2013), which implicitly accounts for the effect of unresolved temperature fluctuations. These values were tabulated in a 2-dimensional array as a function of temperature and contact angle bins with a bin width of 0.1°, as shown in Fig. 1. The right ordinate shows the corresponding dust particle concentrations per contact angle bin taken from Hoyle et al. (2013).

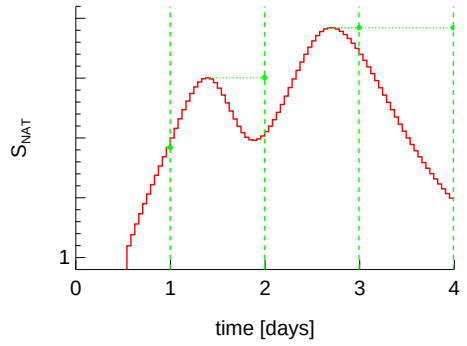

Fig. 2. Schematic of the determination of $S_{\mathrm{NAT}}^{\mathrm{max}}$ along an exemplary air mass trajectory to demonstrate the principle of the parametrisation (no absolute values given). The red line corresponds to the hourly calculated values of S_{NAT} and the green dots indicate the derived value of $S_{\mathrm{NAT}}^{\mathrm{max}}$ for each day of simulation.

To implement this concept into CLaMS, the history of NAT supersaturation of the air parcels is traced from the time when the temperature falls below T_{NAT}. For that, two additional tracers were introduced to the model that represent the maximum supersaturation of HNO_3 over NAT of an air parcel, $S_{\mathrm{NAT}}^{\mathrm{max}}$, and the corresponding temperature T_{min}. Tracing $S_{\mathrm{NAT}}^{\mathrm{max}}$ and T_{min} along the air parcel trajectory has two reasons. First, $S_{\mathrm{NAT}}^{\mathrm{max}}$ and T_{min} are evaluated on an hourly basis whereas the nucleation of NAT particles is decided on a daily basis. The higher time resolution improves the temperature information and increases the possibility to capture temperature minima or maxima. Second, each combination of $S_{\mathrm{NAT}}^{\mathrm{max}}$ and T_{min} represents a certain contact angle bin and is needed to decide whether or not additional NAT particles are nucleated. Only if S_{NAT} increases above the value of $S_{\mathrm{NAT}}^{\mathrm{max}}$ 24 h before, additional NAT particles are nucleated. The number of NAT particles remains constant for $S_{\mathrm{NAT}}^{\mathrm{max}}$ equal or smaller $S_{\mathrm{NAT}}^{\mathrm{max}}$ 24 h before. This is a major difference to the constant nucleation rate approach, which leads to a continuous formation of new particles as long as S_{NAT} is larger than unity. The nucleation rate is determined by summing up the tabulated particle concentrations in the bins of newly activated contact angles, which correspond to a certain combination of temperature and supersaturation (see Fig. 1). Figure 2 is a schematic that illustrates the determination of $S_{\mathrm{NAT}}^{\mathrm{max}}$. The hourly calculated values of S_{NAT} are indicated as a red line and the daily determined values of $S_{\mathrm{NAT}}^{\mathrm{max}}$ as green dots. For this arbitrary example, no additional NAT particles would be nucleated on the last day. Due to the strong non-linearity of the nucleation rate with respect to temperature, we assume that the NAT nucleation rate over one day is dominated by the hour with highest S_{NAT} during the day where the corresponding dust particles are activated and we neglect the nucleation during the rest of the day. As the location of the start of a particle trajectory in general does not coincide with the air parcel, the parametrised nucleation rate is then interpolated onto the locations of NAT particle nucleation in the model. The NAT nucleation rate is then reflected in the NAT number density that is assigned to each individual NAT particle trajectory.

Table 1. Sensitivity simulations performed with CLaMS and corresponding labels. Different horizontal resolutions and assumptions for the NAT nucleation rate J are indicated.

Label	Resolution	Description
HR	70 km	J (this work)
LR	100 km	J (this work)
T+1K	100 km	1 K higher temperatures, J (this work)
T-1K	100 km	1 K lower temperatures, J (this work)
S64	100 km	higher density of particle parcels
Jconst	100 km	constant $J = 8 \times 10^{-6}\,\mathrm{cm}^{-3}\,\mathrm{h}^{-1}$
Jconstx10	100 km	constant $J = 8 \times 10^{-5}\,\mathrm{cm}^{-3}\,\mathrm{h}^{-1}$

2.3 Sensitivity simulations

To evaluate the dependence of the results on details of this parametrisation and to compare the results with previous simulations, sensitivity simulations were performed, by varying the model parameters. The labels of these sensitivity simulations given in the discussion below are listed in Table 1. As indicated above, CLaMS simulations were performed either with a high resolution of 70 km north of 10° N (HR) or with a lower resolution of 100 km north of 40° N (LR). Since the distribution of NAT particle sizes in the simulation is given by particle parcels, each representing a single size, it is not clear whether the chosen density of the particle parcels does successfully represent the properties of all NAT particles. To examine this possible under-sampling, a simulation was performed in which the density of NAT particle parcels nucleated each day was increased from 4 to 64 per air parcel (S64). In turn, the corresponding density assigned to each particle parcel was decreased by a factor of 16. For comparison with earlier publications we included also a simulation with constant NAT nucleation rate of $8 \times 10^{-6}\,\mathrm{cm}^{-3}\,\mathrm{h}^{-1}$ (Jconst) as used by Grooß et al. (2005), as well as a simulation with the constant NAT nucleation rate increased by a factor of 10 (Jconstx10). Since the simulated nucleation and growth of the NAT particles strongly depend on temperature, we also included two sensitivity simulations, in which the ERA-Interim temperatures were decreased and increased by 1 K, respectively (T-1K, T+1K).

3 CLaMS results

3.1 Comparison with H_2O and HNO_3 observations

For the simulation of NAT particles it is important to have realistic H_2O and HNO_3 mixing ratios in the simulation. From Hanson and Mauersberger (1988) it can be derived that for typical polar stratospheric conditions, an increase of

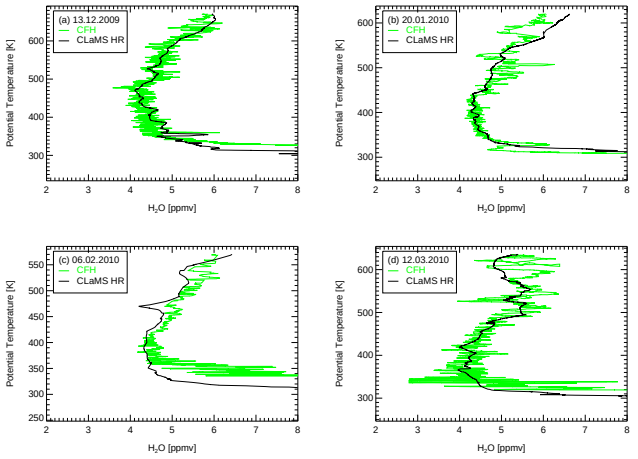

Fig. 3. Comparison of CLaMS H_2O mixing ratios (black) with balloon borne CFH observations (green) made from Sodankylä for different times throughout the winter. Shown are ascent profiles from 13 December 2009, 20 January, 6 February, and 12 March 2010.

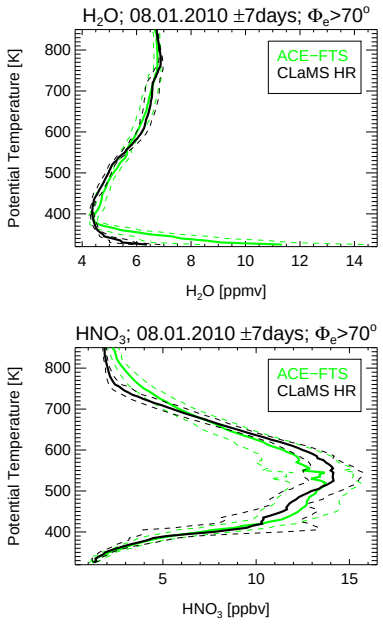

Fig. 4. Comparison of CLaMS H_2O and HNO_3 mixing ratios (black) with ACE-FTS observations (green). The ACE-FTS data is the average of all available data profiles within the time range of 8 January 2010 ± 7 days and with equivalent latitudes greater than 70° N. The dashed lines correspond to the standard deviation of the modelled and measured data ($\pm 1\sigma$, black and green, respectively).

0.5 ppmv H_2O or 3 ppbv HNO_3 introduces a comparable increase to S_{NAT} as a 1 K temperature decrease. Thus, we compared the simulated H_2O and HNO_3 mixing ratios with observations from the balloon based cryogenic frost point hygrometer (CFH), and the satellite based ACE-FTS.

Figure 3 shows four representative comparisons of the model results with balloon based CFH observations made throughout the winter, from Sodankylä, Finland (Vömel et al., 2007; Khaykin et al., 2013). Although CLaMS lacks the vertical resolution to reproduce the very fine structure seen in the observations, the large-scale features are very well reproduced. The rapid decrease in water vapour above about 300 K is represented well in the model, with only the modelled profile in panel c placing this decrease about 25 K too low. At higher potential temperatures, the model again simulates the increasing water vapour with altitude very well, and even the greater variability of the vertical profile on the 12 March 2010, as shown in panel d, appears to be captured to some extent in the CLaMS simulations.

Figure 4 shows the satellite observations of H_2O and HNO_3 obtained by ACE-FTS (average and standard deviation) for the equivalent latitudes greater than 70° N and time range 8 January 2010 ± 7 days and the corresponding co-located simulated mixing ratios. This is the first time period during the simulation where ACE-FTS observations for the vortex core are available due to latitude coverage of the satellite. Again, CLaMS reproduces the observed water vapour values very well at potential temperatures above about 380 K but does have an underestimation by about a factor of 2 at the lower boundary.

The case is similar in the comparison with the ACE-FTS HNO_3 measurements. CLaMS captures the general shape and variability of the observed profile very well. There is some underestimation of HNO_3 at the top of the profile likely due to deviations of the upper boundary values of NO_y. There are also small deviations of modelled water vapour from the observations at low altitudes. However, both deviations are in an altitude region which will not influence PSC formation. Since CLaMS is able to reproduce the observed H_2O and HNO_3 fields in the lower stratosphere, we expect no significant deviations of the derived nucleation rate or PSC properties due to the uncertainty in gas-phase H_2O and HNO_3.

3.2 Particle size distributions

During the RECONCILE Geophysica campaign, in situ observations of PSCs were obtained during five flights in late January 2010. The size distributions of the PSCs were measured in situ on the Geophysica by the experiments FSSP-100 (1.9–38 µm diameter) and FSSP-300 (0.4–24 µm diameter) (Baumgardner et al., 1992; Borrmann et al., 2000a). Here, we compare the NAT particle simulations with the FSSP observations. Figure 5 shows a comparison with the observations between 11:36 and 11:51 UTC on 22 January 2010. This was the period with the largest particle counts for particles larger than 1 µm diameter. The length of this flight path segment is 167 km at a potential temperature level of 425 K. For the determination of the particle size distribution from CLaMS, the particle parcels within a certain volume need to be combined. The model sample volume over which the particle parcels are gathered and included in

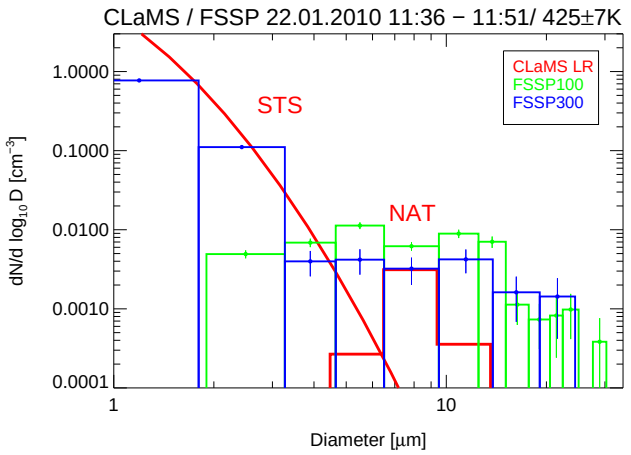

Fig. 5. Particle size distribution from FSSP observations on 22 January 2010. Shown are both FSSP-100 and FSSP-300 data for the flight segment between 11:36 and 11:51 UTC which had one of the largest particle concentrations during this campaign. The corresponding CLaMS particle size distribution (red) has two components, the liquid STS peak and the NAT particle combined from all CLaMS NAT particles within 100 km of the flight path segment.

the composition of the size distribution is defined here by up to 100 km distance within this flight path segment and within ±0.5 model level thickness. For this case, the sample volume contains 38 particle parcels. The diameter size bins for CLaMS is chosen to correspond to those provided by FSSP. The sum of all particle densities in the individual particle size bins is divided by the total number of air parcels in the considered sample volume. The FSSP size distribution should be equal to the sum of the NAT and the STS size distributions. The CLaMS results in Fig. 5 show the log-normal distributions assumed for the liquid ternary aerosol as well as the histogram of the NAT particle size distribution. Observations include the FSSP-100 (green) and the FSSP-300 (blue) channel. The log-normal peak of the modelled liquid aerosol corresponds well with the FSSP-300 data that have the better resolution than FSSP-100 towards the smaller particle diameter, although the particle phase cannot be derived from FSSP. In the 5–10 µm range, the model reproduces measured results, although somewhat underestimates the particle numbers. Although in the CLaMS simulations, larger NAT particles than during the time of the Geophysica observations do occur in other periods of the winter, reaching median diameters of up to 20 µm, none of these large particles observed on board the Geophysica were present in the model for the time and location of the observational data.

The part of the observed size distribution with very large particles exceeding about 15 µm in diameter is not present in the simulations as well as not in any of the sensitivity runs. Here the particles are assumed to be compact spheres. One possible cause for the missing large particles in the simulation could be that the particles are non-spherical (Woiwode, 2013; Borrmann et al., 2000b), which could lead to an overestimation of the observed sizes of some of the particles which were detected with orientations associated with maximum scattering cross sections.

3.3 CALIOP particle classification

A direct comparison of the particles simulated by CLaMS with the CALIOP observations was obtained by simulating the optical signals that would have been caused by the CLaMS particle size distributions. For that purpose, the CLaMS particle size distribution was determined as above for points along the CALIPSO orbit path in the following way: for CALIOP observation profiles with 25 km along track spacing and 180 m vertical spacing, all CLaMS particle parcels within a reference volume were combined. This reference volume was chosen such that it is of the order of the average volume of an air parcel in the simulation. This volume is chosen here vertically by one model layer thickness and horizontally by 50 km distance from the point of observation.

From that volume, a particle size distribution with 15 size bins between 0.8 and 28 µm diameter was determined. In addition, the simulated liquid aerosol particles are characterised by a log-normal distribution. Note that the derived size distributions for neighbouring points are not independent as their reference volumes overlap.

From these particle size distributions, we calculated aerosol backscatter ratios and perpendicular backscatter signals using Mie and T-matrix calculations (Mishchenko et al., 2010). The refractive index for STS was assumed to be 1.44 (Krieger et al., 2000). For NAT, a fixed refractive index of 1.48 was chosen, as used in several earlier studies (Carslaw et al., 1998; Voigt et al., 2003; Luo et al., 2003; Fueglistaler et al., 2003). However, this value is associated with uncertainty and the literature offers a slightly broader range of possible values (e.g. Middlebrook et al., 1994; Toon et al., 1994; Deshler et al., 2000; Biermann et al., 2000). Furthermore, we treat NAT particles as prolate spheroids with aspect ratios of 0.9 (diameter-to-length ratio). Liu and Mishchenko (2001) recommended an aspect ratio smaller 0.83, whereas Daerden et al. (2007) and Scarchilli et al. (2005) used 0.95. We achieve the best agreement with CALIOP measurements using an aspect ratio of 0.9, which yields high values of depolarization. Increasing asphericity, which is in our nomenclature equal to decreasing aspect ratios, results in lower values of the perpendicular backscatter coefficient (see Fig. 7 in Flentje et al., 2002). We performed further T-matrix calculations with aspect ratios of 0.8 and 0.7 (not shown). The agreement between CALIOP and the CLaMS simulations got worse with respect to the perpendicular backscatter, whereas a change in aspect ratio effects backscatter ratios, often dominated by liquid particles, to a smaller degree.

Figures 6 and 7 show CALIOP measurements for two selected orbits on 21 and 30 December, respectively, as well as

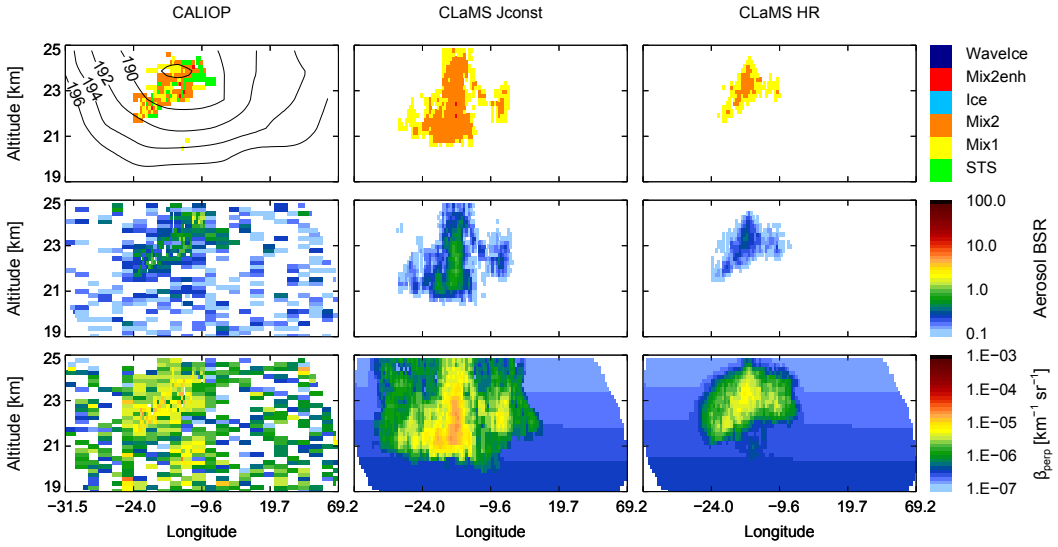

Fig. 6. CALIOP signals for one orbit segment on 21 December 2009, 04:54–04:55 UTC and corresponding T-matrix calculations from CLaMS results. The plots of left column show the CALIOP data, whereas the corresponding CLaMS results for the runs Jconst and HR are shown in the middle and right columns, respectively. The panels in the top row show the particle classification after Pitts et al. (2009). The panels in the middle row correspond to the aerosol backscatter signal. The panels in the lower row correspond to the perpendicular backscatter signal. The temperature (K) from ERA-Interim is indicated by the contour lines in the top left panel.

the corresponding T-matrix calculations for the CLaMS results. CLaMS results are presented for the simulations Jconst and HR. The observation on 21 December corresponds to a time when temperatures were low enough to allow the existence of NAT particles for the first few days. The general location of the PSC and its composition are reproduced by both simulations. However, the dimensions of the simulated NAT clouds differ. Whereas the extent of the NAT cloud simulated by HR seems to be slightly underestimated, Jconst with the constant nucleation rate overestimates the size of the PSC. Both simulations for the CALIOP observation on 30 December overestimate the extent of the PSC, however, the simulation Jconst overestimates the observed area covered by PSCs to a far greater degree.

A comparison based on all available CALIOP data between 21 and 30 December 2009 is shown in Fig. 8. The comparison is limited to December 2009 since ice PSCs have been detected by CALIOP afterwards. The top panel displays the ratio between the observed and simulated cloud fraction (CF) per day. On 21 December, the HR and LR simulations underestimate the observed CF. CF for T+1K is equal to zero until 25 December and below the scale of the figure until 29 December. On 21 December, Jconst already has a modelled area of PSC seven times greater than that observed. All simulations show a trend towards higher CF with proceeding time. On 30 December, all simulations overestimate the cloud coverage by at least a factor of two. The only exception is T+1K with a CF close to 0.5. The second and third panel of Fig. 8 illustrate a point-by-point comparison between CALIOP and CLaMS based on the backscatter ratio (BSR) and the perpendicular backscatter signal (β_{perp}). The level of agreement is expressed in terms of σ, which is the uncertainty associated to the CALIOP measurement. The uncertainty scales with the vertical and horizontal averaging of the data ($\Delta_{\mathrm{vertical}}$ and $\Delta_{\mathrm{horizontal}}$, respectively) and can be calculated for β as follows:

$$\sigma(\beta) = \frac{1}{75}\,\beta\,\sqrt{\frac{2.39\times10^{-5}\,\mathrm{km^{-1}sr^{-1}}}{\beta}\times\frac{1500\,\mathrm{km}}{\Delta_{\mathrm{horizontal}}}\times\frac{5\,\mathrm{km}}{\Delta_{\mathrm{vertical}}}} \quad (1)$$

(Hunt et al., 2009; Engel et al., 2013). This translates into an uncertainty for BSR of

$$\sigma(\mathrm{BSR}) = \mathrm{BSR}\times\frac{\sqrt{\sigma^2(\beta_{\mathrm{perp}})+\sigma^2(\beta_{\mathrm{para}})}}{\beta_{\mathrm{perp}}+\beta_{\mathrm{para}}}. \quad (2)$$

We determined the difference in BSR and β_{perp} between CALIOP and CLaMS for every data point separately and expressed this difference as a fraction of σ. Daily median values are shown for the different simulations. Only data points with temperatures less than 196 K have been considered to reduce the cloudless background. However, the ratio between cloudy and cloudless areas is still unbalanced and the median is dominated by the background values, which tend to be lower in the simulation than in the measurement. Nevertheless, the area covered by clouds increases towards the end of the month and so does the deviation between measurement and simulation. Most prominent are the increasing deviations for the Jconst and T-1K simulations. This comparison could not be extended to the observations in January, since ice particle parcels are not considered in the simulation.

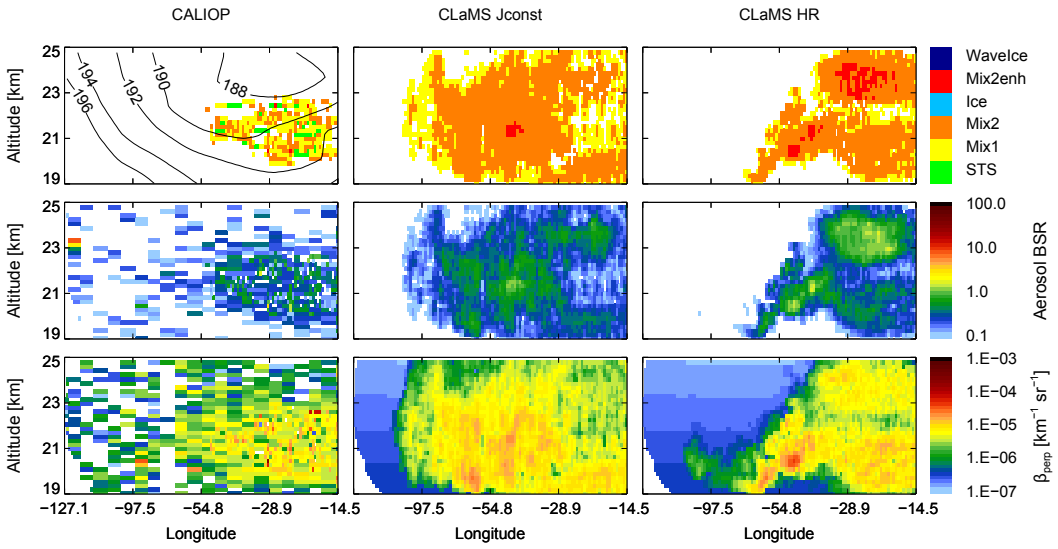

Fig. 7. As Fig. 6, but for 30 December 2009, 12:59 UTC.

3.4 Vertical redistribution of NO_y

The vertical NO_y redistribution is a direct consequence of the sedimentation of NAT particles. The vertical flux of HNO_3 associated with this sedimentation strongly depends on the size and number of the NAT particles and therefore on the parametrisation of the NAT nucleation rate. Figure 9 shows the vertical HNO_3 flux for the cold time period between late December 2009 and end of January 2010 for the different sensitivity simulations. This flux is evaluated at the 463 K model level for the area where NAT particles were present in the model. The results for the simulations HR and LR are almost identical. They agree also with those of S64 (not shown). This shows that the calculated mean HNO_3 flux does not significantly depend on model resolution or the chosen density of model NAT particle parcels. However, significant differences of HNO_3 flux to the other sensitivity simulations occur especially in the early phase (20–25 December) and the late phase (20–30 January). In the simulations with lower temperatures (T-1K) and with constant nucleation rate (Jconstx10 and Jconst), the onset of HNO_3 flux in late December is earlier and the HNO_3 flux is larger than in the simulation HR for the first 10 days. Differences are also larger towards the end of the cold period. For some sensitivity simulations (Jconst, T-1K) the HNO_3 flux is smaller than in the high-resolution run (HR). Differences in the HNO_3 flux in the beginning of the NAT period correspond to differences in the nucleation rate such that a larger nucleation rate causes a larger flux. However, the formation of NAT is slowed down later as less HNO_3 is available due to earlier denitrification.

The resulting amount of denitrification or nitrification can be deduced by subtracting the passive tracer NO_y^* from the simulated NO_y. The vortex core average of this difference is shown in Fig. 10 as a function of time and the vertical coordinate ζ for the high resolution run (HR). Clearly visible is the development of a denitrification region above about 425 K and the nitrification peak below where the NAT particles have evaporated. The maximum simulated denitrification reaches 8.5 ppbv on 19 January near 500 K potential temperature. The maximum simulated nitrification was 6 ppbv on 21 January near 400 K potential temperature.

The differences in the vertical NO_y redistribution throughout all simulations is shown in Fig. 11 for two exemplary days. The patterns of denitrification and nitrification are very similar, with the main differences between the model runs being in the magnitude of the denitrification and nitrification, and not in its altitude. The results show that larger NAT nucleation rates correspond to slightly larger amounts of denitrification and nitrification. Due to the lower temperatures in the simulation T-1K, the particles can sediment longer with the consequence that the nitrification peak is about 20 K lower. Conversely, the nitrification peak of the simulation T+1K is about 20 K higher. Around 425 K in mid-February, the patterns of denitrification and nitrification at individual locations vary within the sensitivity simulations (not shown). But average profiles (e.g. within the vortex core) are very similar. Especially later in the winter, the difference between the different sensitivity simulations becomes smaller. This compensation is likely due to the fact that the formation of NAT may be slowed down for air masses with less available HNO_3 due to earlier denitrification. This can be seen in the T+1 simulation in Fig. 9, in which the onset of the HNO_3 flux is about one week later, but that does have higher HNO_3 fluxes after 15 January, likely because more HNO_3 is still available for NAT formation. The effect of additional HNO_3 transport caused by NAT nucleation on ice particles that has been neglected here may increase the HNO_3 flux in January but could also be reduced by this compensation.

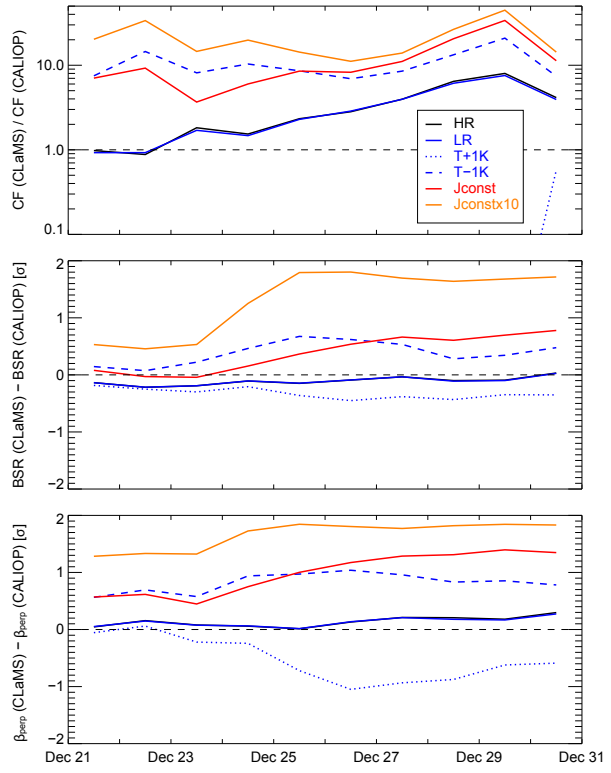

Fig. 8. Comparison of simulated optical properties from CLaMS with CALIOP observations between 21 and 30 December 2009. Upper panel: ratio between observed and simulated cloud fraction (CF) per day. Central panel: point-by-point comparison between CALIOP and CLaMS backscatter ratios (BSR). The level of agreement is expressed as daily median value in terms of σ, which is the uncertainty associated to the CALIOP measurement. See main text for a detailed description of σ. Lower panel: same as central panel but for the perpendicular backscatter signal (β_{perp}).

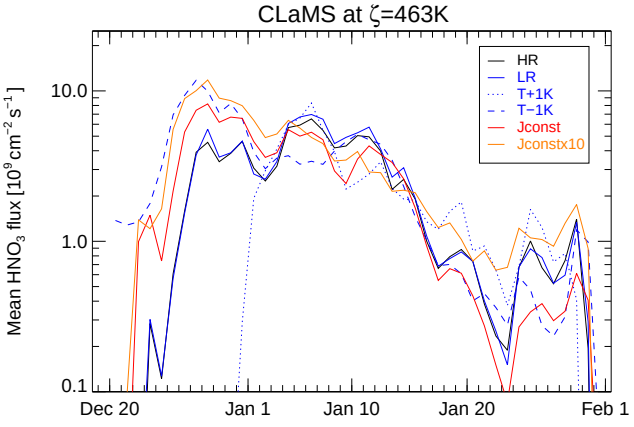

Fig. 9. Calculated mean HNO_3 flux within the model level at 463 K for the cold period between late December and end of January. Shown are the results for the different sensitivity simulations indicated by the line colours and styles as in Fig. 8

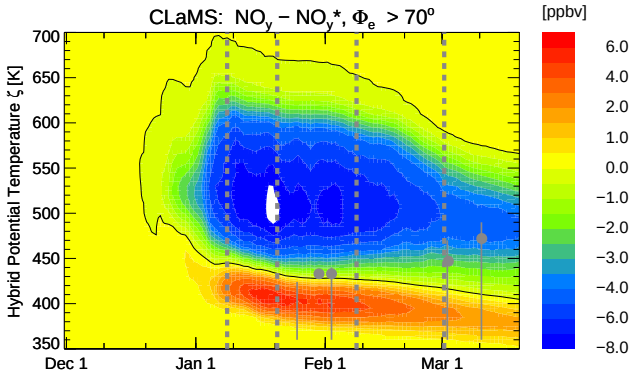

Fig. 10. Simulated NO_y redistribution from CLaMS HR run derived as the difference of simulated NO_y and the passive tracer NO_y^* averaged inside the polar vortex core (equivalent latitudes > 70° N). Thick grey lines indicate dates for which comparisons with ACE-FTS were performed as shown in Fig. 12. Comparisons with SIOUX on Geophysica shown in Figs. 13 and 14 are marked as grey dots and thin grey vertical lines, respectively.

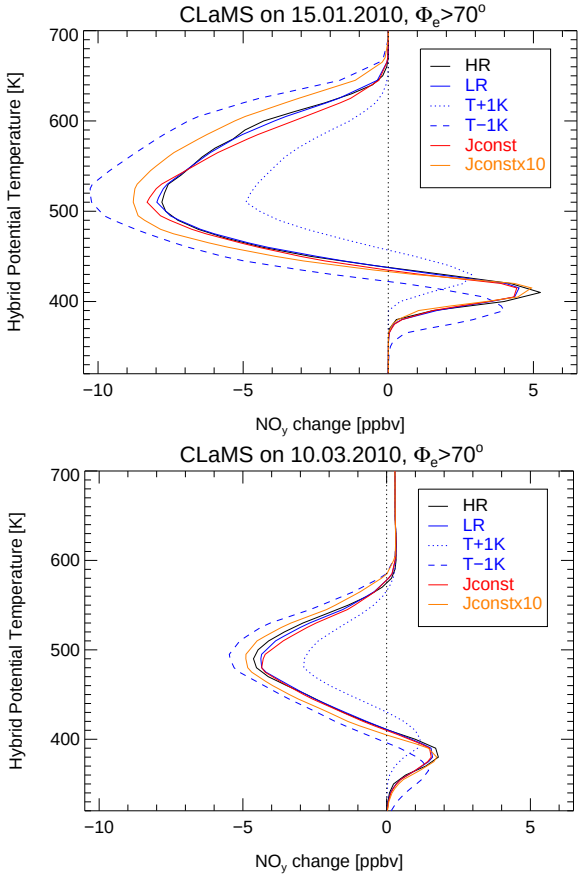

Fig. 11. Simulated NO_y redistribution profiles averaged inside the polar vortex core (equivalent latitudes > 70° N) for 15 January and 10 March. Shown are the results for the different sensitivity simulations as indicated in the legend. Simulation S64 that is almost identical with LR is omitted.

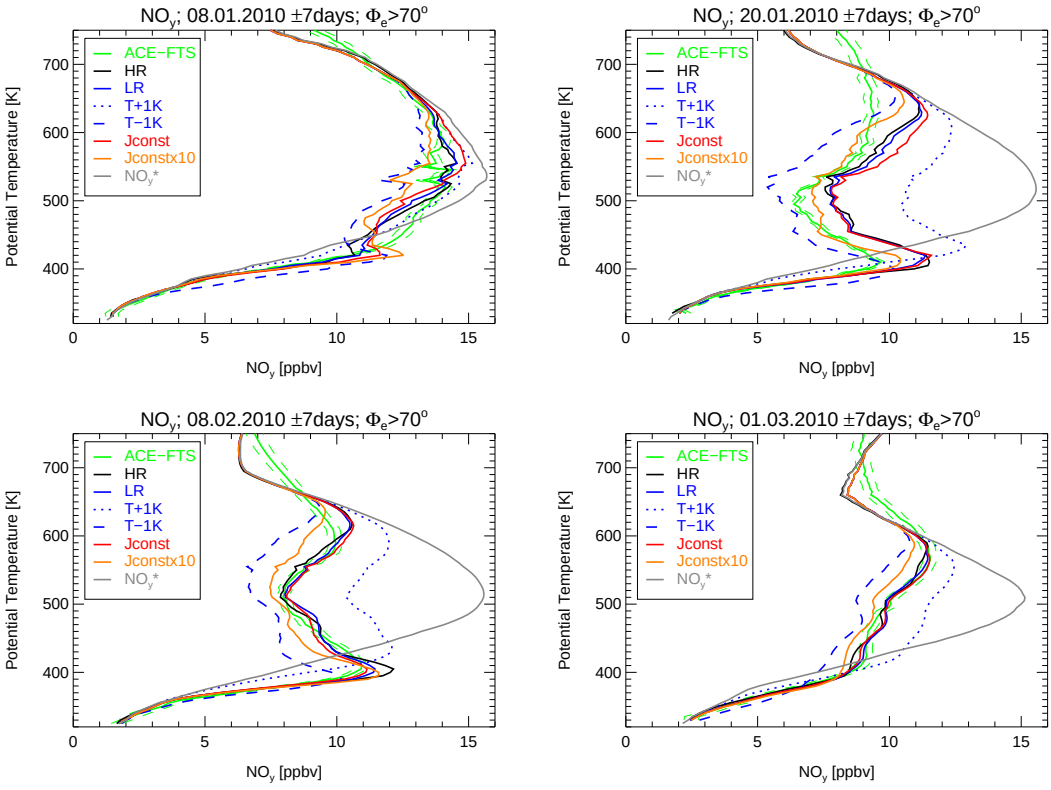

Fig. 12. Comparison of CLaMS NO_y mixing ratios with ACE-FTS data. For 4 different time ranges in which ACE-FTS observations are available in northern polar latitudes, average NO_y profiles from ACE-FTS inside the polar vortex core (equivalent latitudes > 70° N) are shown (green lines). The accuracy of the NO_y data is indicated by the thin dashed green lines. The results for the different sensitivity simulations are indicated by the line colours and styles as in Fig. 8 For comparison, the passive NO_y^* from CLaMS is shown as grey line.

A very useful data set for investigating and evaluating the vertical redistribution of NO_y is the ACE-FTS satellite experiment (Bernath et al., 2005). All major components of NO_y are observed so that the sum NO_y can be determined with high accuracy (Jones et al., 2011). Figure 12 shows the comparison between ACE-FTS version 3.0 and CLaMS for NO_y. Average vortex profiles are shown (equivalent latitudes greater than 70° N) for time intervals with available observations within the vortex core. CLaMS simulations are evaluated for the measurement locations and averaged in the same manner. NO_y mixing ratios lower than the passive tracer NO_y^* mixing ratios (grey line) correspond to denitrification and NO_y mixing ratios higher than NO_y^* to nitrification. Model results for the new nucleation parametrisation as well as for constant nucleation rates are shown, for four time periods in which ACE-FTS observation latitudes cover the Arctic region. In early January, the process of vertical NO_y redistribution starts with less than about 1–2 ppbv denitrification and nitrification. The HR simulation closely reproduced the observed NO_y, with a slight underestimation at around 475 K. The simulation Jconst produced similar results, however, with a slight overestimation at around 575 K and a greater underestimation at 475 K than the simulation HR. Jconstx10 produced a too severe denitrification. During the end of January and early February, a severe denitrification of over 5 ppbv and a distinct nitrification layer is present in both observational and simulated data. For the end of January, the observed profile is best represented by the Jconstx10 simulation, while both HR and Jconst show too much NO_y throughout most of the profile. For mid-February however, HR again provides the best representation of the observations, with Jconst giving very similar results, and Jconstx10 again underestimating the NO_y throughout most of the column. In early March, the signature of the nitrification layer decreased due to mixing with air unaffected by nitrification, whereby the denitrification signature is smoothed out but is still visible. Both simulations HR and Jconst reproduce the observed profile well, with Jconstx10 underestimating NO_y throughout the profile. The deviation of NO_y at the uppermost part of the profile should likely be attributed to inaccuracies of the upper boundary for NO_y.

The simulated NO_y redistribution was also compared with gas-phase in situ NO_y observations made from the Stratospheric Observation Unit for Nitrogen Oxide (SIOUX) aboard the Geophysica aircraft (Voigt et al., 2005). Generally, the SIOUX observations during the RECONCILE

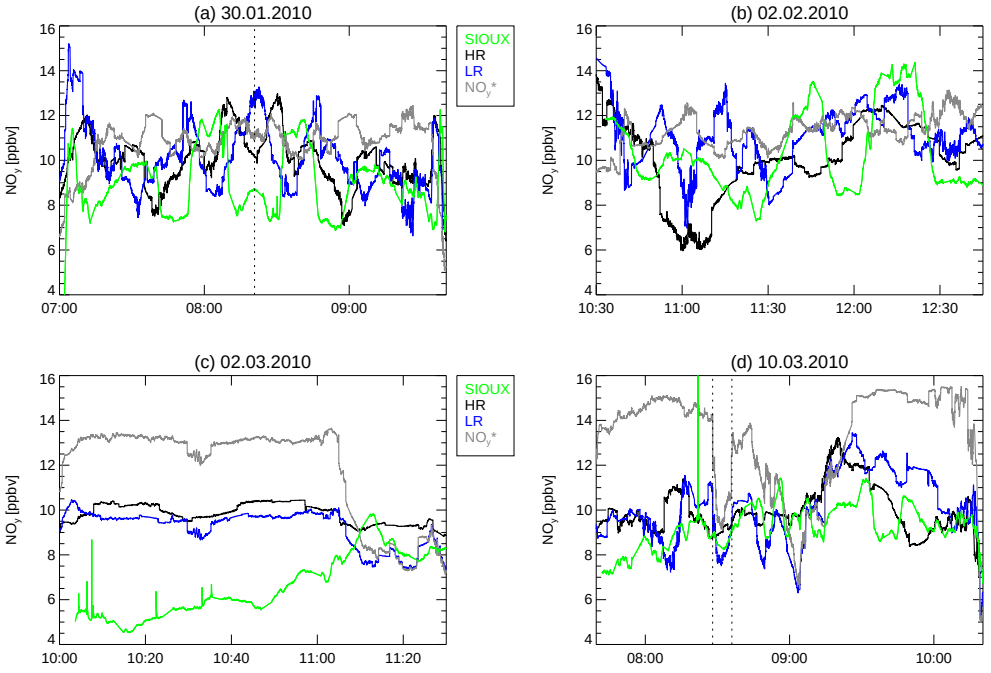

Fig. 13. Comparison of CLaMS NO_y mixing ratios with SIOUX data measured aboard the Geophysica aircraft. Shown are four time sections with NO_y observations inside the vortex for flights on 30 January, 2 February, 2 March and 10 March 2010. SIOUX data are displayed as green lines. CLaMS results are displayed for two different simulations: the high resolution (HR, black) and the low resolution (LR, blue). The passive NO_y^* from CLaMS is shown as grey line. The average potential temperature of the flight segments is 432 K, 433 K, 447 K, and 472 K. In panel a the turnaround time and in panel d the observation of a filament of extra-vortex origin in the vortex (around 8:30 UTC) are marked with dotted lines.

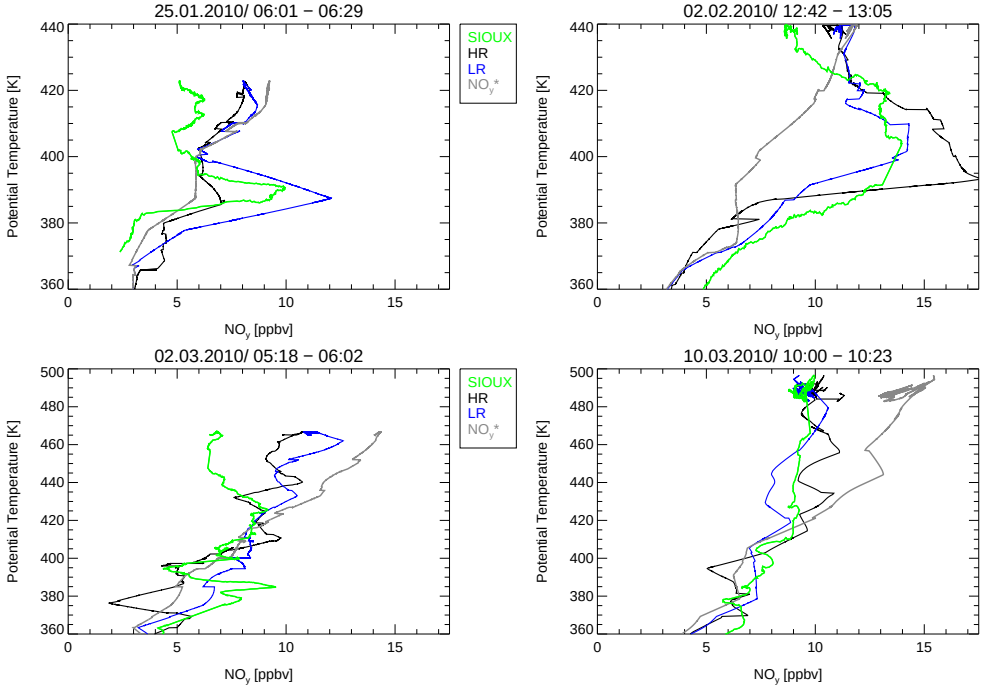

Fig. 14. Comparison of CLaMS NO_y mixing ratio profiles with SIOUX data measured aboard the Geophysica aircraft. Four profiles are shown with NO_y observations inside the vortex for different flights (for date and times see panel titles). SIOUX data are displayed as green lines. CLaMS results are displayed for two different simulations, the high resolution (HR, black) and the low resolution (LR, blue). The passive tracer NO_y^* from CLaMS is shown as a grey line.

campaign show both denitrification and the nitrification layer. An evaluation of the simulated NO_y is however difficult since there are small-scale structures below the model resolution that cannot be reproduced. Figure 13 shows the comparison for four flight segments in which SIOUX NO_y observations within the vortex have been made. The observations are compared with the sensitivity simulations with high and low resolution (HR, LR). The difference between the HR and LR simulations is most noticeable in this comparison. The flights on 30 January and 2 February are located at the transition between the denitrification and the nitrification region (compare Fig. 10). The flight on 30 January was the so-called self-match flight (Sumińska-Ebersoldt et al., 2012) that attempted to probe the same air masses twice resulting in mirroring data structures before and after about 08:20 UTC (dotted line Fig. 13a). The symmetry before and after the turnaround point is visible in the data and also in the model results. For 30 January and 2 February, a very detailed small-scale structure of NO_y is visible both in the observations and in the model. However, the small-scale structure is not reproduced in detail and also the individual sensitivity runs show different structures among themselves. Especially, significant differences can be seen between the runs with different spatial resolutions (HR, LR) that is not seen in the other comparisons. Even in the HR run, the smallest structures in this region cannot be resolved in every detail, probably because small differences in winds or temperatures below the accuracy or in between the 6 h timestep of the ERA-Interim data cause relevant differences in the location of particle evaporation. Also, the NAT nucleation on ice particles could contribute to changes in the small-scale structures of NO_y. It should be noted however, that the global results as zonal mean or vortex mean profiles of NO_y or HNO_3 flux agree quite well for the two resolutions. On 2 March, a vortex remnant was observed in the vicinity of Spitsbergen between about 10:00 and 11:00 UTC, where all the performed simulations underestimate the observed denitrification. On 10 March, when observations within the vortex were taken at somewhat higher potential temperature, the results of the different simulations are closer together and comparable with the observations. Between about 08:50 and 09:20 UTC, the observations are located outside the vortex. A filament of extra-vortex air that was recently drawn into the vortex (Hösen, 2013) marked by the dotted lines shows little denitrification.

The altitude dependence of the NO_y redistribution is shown similarly in Fig. 14 for flights on 4 different days with altitude profiles containing the nitrification peak. The simulations reproduce the general features like the denitrification region and the nitrification peak. However, the small-scale variability can not be reproduced in every detail as explained above. The evaluation of the simulated vertical NO_y redistribution and the comparison with ACE-FTS and SIOUX data indicates that the sensitivity on the choice of nucleation rate parametrisation in early March is less pronounced than in January.

4 Conclusions

We have shown global model simulations of NAT particle nucleation, particle growth, sedimentation and resulting denitrification. For the first time, a temperature-dependent NAT nucleation rate, derived from CALIOP observations (Hoyle et al., 2013; Engel et al., 2013) has been applied to a global chemical transport model. The processes leading to denitrification have been compared with observations including CALIOP particle classification, observed size distributions and observations of NO_y and its compounds by various observational techniques and platforms.

The comparisons show that the general behaviour of the presented observations is reproduced by the simulations. The location and extent of the observed NAT PSCs as seen in the CALIOP data from December 2009 are better reproduced by the new nucleation scheme than by using a constant nucleation rate. The constant nucleation rate overestimates cloud coverage as well as single optical cloud properties significantly. We leave a comparison between CLaMS and PSCs observed in January 2010 open. So far, ice particles are not accounted for in the Lagrangian sedimentation scheme, but have been observed after 31 December 2009. A detailed cloud comparison requires further model development and research. Despite the lack of a NAT nucleation mechanism, which involves pre-existing ice particles, and further uncertainties referring to model temperatures and particle shapes, the vortex averaged NO_y profiles observed by ACE-FTS can be simulated satisfactorily throughout the entire winter by all model configurations. The temporal evolution of the NO_y flux demonstrates larger NO_y fluxes in the early winter for the simulations Jconst and T-1K than for HR and LR. However, this effect is compensated by less pronounced fluxes in late January. As a net effect, averaged NO_y profiles in late winter look similar. Only the upper and lower extrema of the sensitivity runs, namely T+1K and T-1K under and overestimate the denitrification in late winter, respectively.

We propose to use the new parametrisation in future studies of PSC formation and denitrification since numerical costs are comparable to the usage of a constant nucleation rate. The overall denitrification at the end of the Polar winter might be as well reproduced by a constant nucleation rate as by the new parametrisation. However, a NAT saturation dependent parametrisation allows for a much more detailed comparison in terms of PSC occurrence and composition.

Table A1. Reactions included into the CLaMS chemistry. Only the additional reactions are listed, which were not described by McKenna et al. (2002b), from which the bimolecular reactions (B1–B64), trimolecular or thermal decomposition reactions (T1–T12), photolysis reactions (J1–J27) and heterogeneous reactions (H1–H11) are used. Carbon and Fluorine containing products from halocarbon decomposition are neglected.

Nr	Reaction		
B65	$H + O_3$	$\rightarrow$	$OH + O_2$
B66	$H + HO_2$	$\rightarrow$	$OH + OH$
B67	$H + HO_2$	$\rightarrow$	$H_2O + O(^3P)$
B68	$H + HO_2$	$\rightarrow$	$H_2 + O_2$
B69	$H_2 + OH$	$\rightarrow$	$H_2O + H$
B70	$OH + O(^3P)$	$\rightarrow$	$H + O_2$
B71	$OH + OH$	$\rightarrow$	$H_2O + O(^3P)$
B72	$HO_2 + O(^3P)$	$\rightarrow$	$OH + O_2$
B73	$H_2O_2 + O(^3P)$	$\rightarrow$	$OH + HO_2$
B74	$O(^3P) + HOCl$	$\rightarrow$	$OH + ClO$
B75	$N_2O + O(^1D)$	$\rightarrow$	$N_2 + O_2$
B76	$N_2O + O(^1D)$	$\rightarrow$	$NO + NO$
B77	$CCl_3F + O(^1D)$	$\rightarrow$	$ClO + 2\ Cl + \text{products}$
B78	$CCl_2F_2 + O(^1D)$	$\rightarrow$	$ClO + Cl + \text{products}$
B79	$CHClF_2 + O(^1D)$	$\rightarrow$	$ClO + H + \text{products}$
B80	$CCl_3F_3 + O(^1D)$	$\rightarrow$	$ClO + 2\ Cl + \text{products}$
B81	$CCl_4 + O(^1D)$	$\rightarrow$	$3\ Cl + ClO + \text{products}$
B82	$CHClF_2 + OH$	$\rightarrow$	$Cl + H_2O + \text{products}$
B83	$CH_3Cl + OH\ (+O_2)$	$\rightarrow$	$ClO + CH_3OOH$
T13	$H + O_2 + M$	$\rightarrow$	HO_2
J28	$HCl + h\nu$	$\rightarrow$	$H + Cl$
J29	$H_2O + h\nu$	$\rightarrow$	$H + OH$
J30	$CCl_3F + h\nu$	$\rightarrow$	$3\ Cl + \text{products}$
J31	$CCl_2F_2 + h\nu$	$\rightarrow$	$2\ Cl + \text{products}$
J32	$CHClF_2 + h\nu$	$\rightarrow$	$Cl + H + \text{products}$
J33	$CCl_3F_3 + h\nu$	$\rightarrow$	$3\ Cl + \text{products}$
J34	$CH_3Cl + h\nu\ (+O_2)$	$\rightarrow$	$CH_3OO + Cl$
J35	$CCl_4 + h\nu$	$\rightarrow$	$4\ Cl + \text{products}$
J36	$N_2O + h\nu$	$\rightarrow$	$O(^1D) + N_2$

Appendix A

CLaMS model details

The chemical reaction scheme has been updated with respect to McKenna et al. (2002b) and the additional reactions are listed in Table A1. The polynomial fits of the correlations used in the initialisation and boundary condition are summarised in Table A2.

Table A2. Tracer correlations used in the initialisation procedure. The tracer correlations are derived from the observations using a polynomial fit of the form $[y] = \sum_{i=0}^{n} a_i \cdot [x]^i$ and degree $n \leq 4$. The unit of CH_4 is ppmv, the units of N_2O, Cl_y, NO_y, and CO are ppbv and the unit of Br_y and halocarbons is pptv. For values of $[x]$ outside of the valid range, the closest valid value was used. The correlations are based on ACE-FTS version 3.0 data from October and November 2009 for equivalent latitudes greater then 50° N with the exception of Cl_y and Br_y that are taken from Grooß et al. (2005). The initialisation of $CFCl_3$ (CFC-11) is based on a wider range of equivalent latitudes (Φ_e) given in the third column (in degrees).

$[x]$	$[y]$	Range of Φ_e	Valid range of $[x]$	a_0	a_1	a_2	a_3	a_4
N_2O	CH_4		9.5–330	0.1917	0.01333	-8.239×10^{-5}	2.840×10^{-7}	-3.376×10^{-10}
ln N_2O	CH_4		ln 0.1–ln 9.5	0.1391	0.02516	0.01335	0.004192	0
CH_4	Cl_y		0.498–1.76	2.510	3.517	−3.741	0.4841	0.03042
CH_4	Br_y		0.65–1.64	48.73	−116.9	170.5	−102.1	19.58
N_2O	NO_y		49.6–330	11.57	0.1235	-1.013×10^{-3}	1.984×10^{-6}	-1.119×10^{-9}
ln N_2O	NO_y		ln 0.1–ln 49.6	7.988	1.338	0.1461	0	0
N_2O	CO		240–330	454.05	−8.8606	0.06614	-2.1697×10^{-4}	2.6421×10^{-7}
N_2O	CO		71–240	14.5	0	0	0	0
N_2O	CO		10–71	5.721	0.3647	-6.923×10^{-03}	6.855×10^{-5}	-2.656×10^{-7}
N_2O	CO		0–10	0	0.8740	0	0	0
N_2O	$CFCl_3$	60–90	204–312	−11.20	0.7959	−0.01413	8.508×10^{-5}	-1.278×10^{-7}
N_2O	$CFCl_3$	60–90	125–204	−12.15	0.6649	-8.777×10^{-3}	3.604×10^{-05}	0
N_2O	$CFCl_3$	60–90	100–125	−16.88	0.1688	0	0	0
N_2O	$CFCl_3$	40–60	147.5–326	−242.1	4.719	−0.04039	1.645×10^{-4}	-2.176×10^{-7}
N_2O	$CFCl_3$	20–40	169–320	−273.4	1.618	0	0	0
N_2O	$CFCl_3$	−10–10	216–314	−539.4	2.496	0	0	0
N_2O	CF_2Cl_2		30–312	−2.218	0.5757	7.425×10^{-3}	-1.285×10^{-5}	0
N_2O	CF_2Cl_2		0–30	0	0.7130	0	0	0
N_2O	CH_3Cl		200–330	−390	3.150	0	0	0
N_2O	CH_3Cl		100–200	−240	2.40	0	0	0
N_2O	$CHClF_2$		10–305.5	55.16	0.7999	-2.738×10^{-3}	5.400×10^{-6}	0
N_2O	$CHClF_2$		0–10	0	6.289	0	0	0
N_2O	CCl_4		190–330	−2.065	0.1238	-8.598×10^{-4}	4.805×10^{-6}	0
N_2O	CCl_4		120–190	−40.06	0.3339	0	0	0
N_2O	$C_2Cl_3F_3$		170–330	−83.69	0.4923	0	0	0

Acknowledgements. This work was supported by the RECONCILE project of the European Commission Seventh Framework Programme (FP7) under the Grant number RECONCILE-226365-FP7-ENV-2008-1. We thank S. Fueglistaler and one anonymous reviewer for their constructive remarks. We acknowlege F. Ploeger and P. Konopka for providing the data of the multi-annual CLaMS simulation. We thank L. Poole for providing and explaining the uncertainty estimates of the CALIOP signals. We thank the European Centre of Medium-Range Weather Forecasts (ECMWF) for providing the meteorological data. The ACE mission was funded by the Canadian Space Agency. The authors gratefully acknowledge the computing time granted on the supercomputer JUROPA at Jülich Supercomputing Centre (JSC) under the VSR project ID JICG11. The balloon-borne measurements of water vapour were obtained within the LAPBIAT2 atmospheric sounding campaign that was supported by EU under the IHP Access to Research Infrastructures and the Finnish Academy under grant number 140408. CRH was funded via Swiss National Science Foundation (SNSF) grant number 200021_140663.

The service charges for this open access publication have been covered by a Research Centre of the Helmholtz Association.

Edited by: D. Knopf

References

Baumgardner, D., Dye, J. E., Gandrud, B. W., and Knollenberg, R. G.: Interpretation of measurements made the Forward Scattering Spectrometer Probe (FSSP300) during the Airborne Artic Stratospheric Expedition, J. Geophys. Res., 97, 8035–8046, 1992.

Bernath, P. F., McElroy, C. T., Abrams, M. C., Boone, C. D., Butler, M., Camy-Peyret, C., Carleer, M., Clerbaux, C., Coheur, P.-F., Colin, R., DeCola, P., DeMazière, M., Drummond, J. R., Dufour, D., Evans, W. F. J., Fast, H., Fussen, D., Gilbert, K., Jennings, D. E., Llewellyn, E. J., Lowe, R. P., Mahieu, E., McConnell, J. C., McHugh, M., McLeod, S. D., Michaud, R., Midwinter, C., Nassar, R., Nichitiu, F., Nowlan, C., Rinsland, C. P., Rochon, Y. J., Rowlands, N., Semeniuk, K., Simon, P., Skelton, R., Sloan, J. J., Soucy, M.-A., Strong, K., Tremblay, P., Turnbull, D., Walker, K. A., Walkty, I., Wardle, D. A., Wehrle, V., Zander, R., and Zou, J.: Atmospheric Chemistry Experiment (ACE) Mission overview, Geophys. Res. Lett., 32, L15S01, doi:10.1029/2005GL022386, 2005.

Biermann, U. M., Luo, B. P., and Peter, T.: Absorption spectra and optical constants of binary and ternary solutions of H_2SO_4, HNO_3, and H_2O in the mid infrared at atmospheric temperatures, J. Phys. Chem. A, 104, 783–793, doi:10.1021/jp992349i, 2000.

Borrmann, S., Thomas, A., Rudakov, V., Yushkov, V., Lepuchov, B., Deshler, T., Vinnichenko, N., Khattatov, V., and Stefanutti, L.: Stratospheric aerosol measurements in the Arctic winter of 1996/1997 with the M-55 Geophysika high-altitude research aircraft, Tellus B, 52, 1088–1103, doi:10.1034/j.1600-0889.2000.00100.x, 2000a.

Borrmann, S., Luo, B., and Mishchenko, M.: Application of the T-matrix method to the measurement of aspherical (ellipsoidal) particles with forward scattering optical particle counters, J. Aerosol Sci., 31, 789–799, doi:10.1016/S0021-8502(99)00563-7, 2000b.

Carslaw, K. S., Wirth, M., Tsias, A., Luo, B. P., Dörnbrack, A., Leutbecher, M., Volkert, H., Renger, W., Bacmeister, J. T., and Peter, T.: Particle microphysics and chemistry in remotely observed mountain polar stratospheric clouds, J. Geophys. Res., 103, 5785–5796, 1998.

Carslaw, K. S., Kettleborough, J. A., Northway, M. J., Davies, S., Gao, R., Fahey, D. W., Baumgardner, D. G., Chipperfield, M. P., and Kleinböhl, A.: A vortex-scale simulation of the growth and sedimentation of large nitric acid hydrate particles, J. Geophys. Res., 107, 8300, doi:10.1029/2001JD000467, 2002.

Curtius, J., Weigel, R., Vössing, H.-J., Wernli, H., Werner, A., Volk, C.-M., Konopka, P., Krebsbach, M., Schiller, C., Roiger, A., Schlager, H., Dreiling, V., and Borrmann, S.: Observations of meteoric material and implications for aerosol nucleation in the winter Arctic lower stratosphere derived from in situ particle measurements, Atmos. Chem. Phys., 5, 3053–3069, doi:10.5194/acp-5-3053-2005, 2005.

Daerden, F., Larsen, N., Chabrillat, S., Errera, Q., Bonjean, S., Fonteyn, D., Hoppel, K., and Fromm, M.: A 3D-CTM with detailed online PSC-microphysics: analysis of the Antarctic winter 2003 by comparison with satellite observations, Atmos. Chem. Phys., 7, 1755–1772, doi:10.5194/acp-7-1755-2007, 2007.

Davies, S., Mann, G. W., Carslaw, K. S., Chipperfield, M. P., Kettleborough, J. A., Santee, M. L., Oelhaf, H., Wetzel, G., Sasano, Y., and Sugita, T.: 3-D microphysical model studies of Arctic denitrification: comparison with observations, Atmos. Chem. Phys., 5, 3093–3109, doi:10.5194/acp-5-3093-2005, 2005.

Dee, D. P., Uppala, S. M., Simmons, A. J., Berrisford, P., Poli, P., Kobayashi, S., Andrae, U., Balmaseda, M. A., Balsamo, G., Bauer, P., Bechtold, P., Beljaars, A. C. M., van de Berg, L., Bidlot, J., Bormann, N., Delsol, C., Dragani, R., Fuentes, M., Geer, A. J., Haimberger, L., Healy, S. B., Hersbach, H., Holm, E. V., Isaksen, L., Kallberg, P., Koehler, M., Matricardi, M., McNally, A. P., Monge-Sanz, B. M., Morcrette, J. J., Park, B. K., Peubey, C., de Rosnay, P., Tavolato, C., Thepaut, J. N., and Vitart, F.: The ERA-Interim reanalysis: configuration and performance of the data assimilation system, Q. J. Roy. Meteor. Soc., 137, 553–597, doi:10.1002/qj.828, 2011.

Deshler, T., Nardi, B., Adriani, A., Cairo, F., Hansen, G., Fierli, F., Hauchecorne, A., and Pulvirenti, L.: Determining the index of refraction of polar stratospheric clouds above Andoya (69° N) by combining size-resolved concentration and optical scattering measurements, J. Geophys. Res., 105, 3943–3953, doi:10.1029/1999JD900469, 2000.

Dörnbrack, A., Pitts, M. C., Poole, L. R., Orsolini, Y. J., Nishii, K., and Nakamura, H.: The 2009–2010 Arctic stratospheric winter – general evolution, mountain waves and predictability of an operational weather forecast model, Atmos. Chem. Phys., 12, 3659–3675, doi:10.5194/acp-12-3659-2012, 2012.

Drdla, K. and Müller, R.: Temperature thresholds for chlorine activation and ozone loss in the polar stratosphere, Ann. Geophys., 30, 1055–1073, doi:10.5194/angeo-30-1-2012, 2012.

Engel, I., Luo, B. P., Pitts, M. C., Poole, L. R., Hoyle, C. R., Grooß, J.-U., Dörnbrack, A., and Peter, T.: Heterogeneous formation of polar stratospheric clouds – Part 2: Nucleation of ice on synoptic scales, Atmos. Chem. Phys., 13, 10769–10785, doi:10.5194/acp-13-10769-2013, 2013.

Eyring, V., Butchart, N., Waugh, D. W., Akiyoshi, H., Austin, J., Bekki, S., Bodeker, G. E., Boville, B. A., Brühl, C., Chipperfield, M. P., Cordero, E., Dameris, M., Deushi, M., Fioletov, V. E., Frith, S. M., Garcia, R. R., Gettelman, A., Giorgetta, M. A., Grewe, V., Jourdain, L., Kinnison, D. E., Mancini, E., Manzini, E., Marchand, M., Marsh, D. R., Nagashima, T., Nielsen, E., Newman, P. A., Pawson, S., Pitari, G., Plummer, D. A., Rozanov, E., Schraner, M., Shepherd, T. G., Shibata, K., Stolarski, R. S., Struthers, H., Tian, W., and Yoshiki, M.: Assessment of temperature, trace species and ozone in chemistry-climate simulations of the recent past, J. Geophys. Res., 111, D22308, doi:10.1029/2006JD007327, 2006.

Fahey, D. W., Gao, R. S., Carslaw, K. S., Kettleborough, J., Popp, P. J., Northway, M. J., Holecek, J. C., Ciciora, S. C., McLaughlin, R. J., Thompson, T. L., Winkler, R. H., Baumgardner, D. G., Gandrud, B., Wennberg, P. O., Dhaniyala, S., McKinley, K., Peter, T., Salawitch, R. J., Bui, T. P., Elkins, J. W., Webster, C. R., Atlas, E. L., Jost, H., Wilson, J. C., Herman, R. L., Kleinböhl, A., and von König, M.: The detection of large HNO_3-containing particles in the winter Arctic stratosphere, Science, 291, 1026–1031, 2001.

Flentje, H., Dörnbrack, A., Fix, A., Meister, A., Schmid, H., Fueglistaler, S., Luo, B. P., and Peter, T.: Denitrification inside the stratospheric vortex in the winter of 1999–2000 by sedimentation of large nitric acid trihydrate particles, J. Geophys. Res., 107, AAC 11–1–AAC 11–15, doi:10.1029/2001JD001015, 2002.

Fueglistaler, S., Buss, S., Luo, B. P., Wernli, H., Flentje, H., Hostetler, C. A., Poole, L. R., Carslaw, K. S., and Peter, Th.: Detailed modeling of mountain wave PSCs, Atmos. Chem. Phys., 3, 697–712, doi:10.5194/acp-3-697-2003, 2003.

Grooß, J.-U.: Modelling of Stratospheric Chemistry based on HALOE/UARS Satellite Data, PhD thesis, University of Mainz, 1996.

Grooß, J.-U. and Müller, R.: Simulation of ozone loss in Arctic winter 2004/2005, Geophys. Res. Lett., 34, L05804, doi:10.1029/2006GL028901, 2007.

Grooß, J.-U., Günther, G., Konopka, P., Müller, R., McKenna, D. S., Stroh, F., Vogel, B., Engel, A., Müller, M., Hoppel, K., Bevilacqua, R., Richard, E., Webster, C. R., Elkins, J. W., Hurst, D. F., Romashkin, P. A., and Baumgardner, D. G.: Simulation of ozone depletion in spring 2000 with the Chemical Lagrangian Model of the Stratosphere (CLaMS), J. Geophys. Res., 107, 8295, doi:10.1029/2001JD000456, 2002.

Grooß, J.-U., Günther, G., Müller, R., Konopka, P., Bausch, S., Schlager, H., Voigt, C., Volk, C. M., and Toon, G. C.: Simulation of denitrification and ozone loss for the Arctic winter 2002/2003, Atmos. Chem. Phys., 5, 1437–1448, doi:10.5194/acp-5-1437-2005, 2005.

Hanson, D. R. and Mauersberger, K.: Laboratory studies of the nitric acid trihydrate: Implications for the south polar stratosphere, Geophys. Res. Lett., 15, 855–858, doi:10.1029/GL015i013p01507, 1988.

Hösen, E.: Untersuchung von Transport, Mischung und Ozonverlust in der arktischen Polarregion im Winter 2009/10 basierend auf flugzeuggestützten in-situ-Messungen, Dissertation, Bergische Universität Wuppertal, Germany, 2013.

Hoyle, C. R., Engel, I., Luo, B. P., Pitts, M. C., Poole, L. R., Grooß, J.-U., and Peter, T.: Heterogeneous formation of polar stratospheric clouds – Part 1: Nucleation of nitric acid trihydrate (NAT), Atmos. Chem. Phys., 13, 9577–9595, doi:10.5194/acp-13-9577-2013, 2013.

Hunt, W. H., Winker, D. M., Vaughan, M. A., Powell, K. A., Lucker, P. L., and Weimer, C.: CALIPSO Lidar Description and Performance Assessment, J. Atmos. Ocean. Tech., 26, 1214–1228, doi:10.1175/2009JTECHA1223.1, 2009.

Jones, A., Qin, G., Strong, K., Walker, K. A., McLinden, C., M. Toohey, T., Kerzenmacher, Bernath, P., and Boone, C.: A global inventory of stratospheric NOy from ACE-FTS, J. Geophys. Res., 116, D17304, doi:10.1029/2010JD015465, 2011.

Kalicinsky, C., Grooß, J.-U., Günther, G., Ungermann, J., Blank, J., Höfer, S., Hoffmann, L., Knieling, P., Olschewski, F., Spang, R., Stroh, F., and Riese, M.: Observations of filamentary structures near the vortex edge in the Arctic winter lower stratosphere, Atmos. Chem. Phys., 13, 10859–10871, doi:10.5194/acp-13-10859-2013, 2013.

Khaykin, S. M., Engel, I., Vömel, H., Formanyuk, I. M., Kivi, R., Korshunov, L. I., Krämer, M., Lykov, A. D., Meier, S., Naebert, T., Pitts, M. C., Santee, M. L., Spelten, N., Wienhold, F. G., Yushkov, V. A., and Peter, T.: Arctic stratospheric dehydration – Part 1: Unprecedented observation of vertical redistribution of water, Atmos. Chem. Phys., 13, 11503–11517, doi:10.5194/acp-13-11503-2013, 2013.

Konopka, P., Steinhorst, H.-M., Grooß, J.-U., Günther, G., Müller, R., Elkins, J. W., Jost, H.-J., Richard, E., Schmidt, U., Toon, G., and McKenna, D. S.: Mixing and Ozone Loss in the 1999–2000 Arctic Vortex: Simulations with the 3-dimensional Chemical Lagrangian Model of the Stratosphere (CLaMS), J. Geophys. Res., 109, D02315, doi:10.1029/2003JD003792, 2004.

Konopka, P., Günther, G., McKenna, D. S., Müller, R., Offermann, D., Spang, R., and Riese, M.: How homogeneous and isotropic is stratospheric mixing? Comparison of CRISTA-1 observations with transport studies based on the Chemical Lagrangian Model of the Stratosphere (CLaMS), Q. J. Roy. Meteor. Soc., 131, 565–579, doi:10.1256/qj.04.47, 2005.

Konopka, P., Günther, G., Müller, R., dos Santos, F. H. S., Schiller, C., Ravegnani, F., Ulanovsky, A., Schlager, H., Volk, C. M., Viciani, S., Pan, L. L., McKenna, D.-S., and Riese, M.: Contribution of mixing to upward transport across the tropical tropopause layer (TTL), Atmos. Chem. Phys., 7, 3285–3308, doi:10.5194/acp-7-3285-2007, 2007.

Krämer, M., Schiller, C., Afchine, A., Bauer, R., Gensch, I., Mangold, A., Schlicht, S., Spelten, N., Sitnikov, N., Borrmann, S., de Reus, M., and Spichtinger, P.: Ice supersaturations and cirrus cloud crystal numbers, Atmos. Chem. Phys., 9, 3505–3522, doi:10.5194/acp-9-3505-2009, 2009.

Krieger, U. K., Mössinger, J. C., Luo, B. P., Weers, U., and Peter, T.: Measurement of the refractive indices of H_2SO_4-HNO_3-H_2O solutions to stratospheric temperatures, Appl. Optics, 39, 3691–3703, doi:10.1364/AO.39.003691, 2000.

Liu, L. and Mishchenko, M. I.: Constraints on PSC particle microphysics derived from lidar observations, J. Quant. Spectrosc. Ra., 70, 817–831, doi:10.1016/S0022-4073(01)00048-6, 2001.

Luo, B. P., Voigt, C., Fueglistaler, S., and Peter, T.: Extreme NAT supersaturations in mountain wave ice PSCs: A clue to NAT formation, J. Geophys. Res., 108, 4443, doi:10.1029/2002JD003104, 2003.

McKenna, D. S., Konopka, P., Grooß, J.-U., Günther, G., Müller, R., Spang, R., Offermann, D., and Orsolini, Y.: A new Chemical Lagrangian Model of the Stratosphere (CLaMS): 1. Formulation of advection and mixing, J. Geophys. Res., 107, 4309, doi:10.1029/2000JD000114, 2002a.

McKenna, D. S., Grooß, J.-U., Günther, G., Konopka, P., Müller, R., Carver, G., and Sasano, Y.: A new Chemical Lagrangian Model of the Stratosphere (CLaMS): 2. Formulation of chemistry scheme and initialization, J. Geophys. Res., 107, 4256, doi:10.1029/2000JD000113, 2002b.

Middlebrook, A. M., Berland, B. S., George, S. M., Tolbert, M. A., and Toon, O. B.: Real refractive indices of infrared-characterized nitric-acid/ice films: Implications for optical measurements of polar stratospheric clouds, J. Geophys. Res., 99, 25655–25666, doi:10.1029/94JD02391, 1994.

Mishchenko, M. I., Travis, L. D., and Mackowski, D. W.: T-matrix computations of light scattering by nonspherical particles: a review, J. Quant. Spectrosc. Ra., 111, 1704–1744, 2010.

Müller, R., Peter, T., Crutzen, P. J., Oelhaf, H., Adrian, G. P., v. Clarmann, T., Wegner, A., Schmidt, U., and Lary, D.: Chlorine chemistry and the potential for ozone depletion in the Arctic stratosphere in the winter of 1991/92, Geophys. Res. Lett., 21, 1427–1430, 1994.

Nickolaisen, S. L., Friedl, R. R., and Sander, S. P.: Kinetics and Mechanism of the ClO+ClO Reaction – Pressure and Temperature Dependences of the Bimolecular and Termolecular Channels and Thermal-Decomposition of Chlorine Peroxide, J. Phys. Chem., 98, 155–169, 1994.

Papanastasiou, D. K., Papadimitriou, V. C., Fahey, D. W., and Burkholder, J. B.: UV Absorption Spectrum of the ClO Dimer (Cl_2O_2) between 200 and 420 nm, J. Phys. Chem. A, 113, 13711–13726, 2009.

Pitts, M. C., Poole, L. R., and Thomason, L. W.: CALIPSO polar stratospheric cloud observations: second-generation detection algorithm and composition discrimination, Atmos. Chem. Phys., 9, 7577–7589, doi:10.5194/acp-9-7577-2009, 2009.

Pitts, M. C., Poole, L. R., Dörnbrack, A., and Thomason, L. W.: The 2009–2010 Arctic polar stratospheric cloud season: a CALIPSO perspective, Atmos. Chem. Phys., 11, 2161–2177, doi:10.5194/acp-11-2161-2011, 2011.

Plenge, J., Kühl, S., Vogel, B., Müller, R., Stroh, F., von Hobe, M., Flesch, R., and Rühl, E.: Bond strength of chlorine peroxide, J. Phys. Chem. A, 109, 6730–6734, 2005.

Ploeger, F., Konopka, P., Günther, G., Grooß, J.-U., and Müller, R.: Impact of the vertical velocity scheme on modeling transport across the tropical tropopause layer, J. Geophys. Res., 115, D03301, doi:10.1029/2009JD012023, 2010.

Ploeger, F., Günther, G., Konopka, P., Fueglistaler, S., Müller, R., Hoppe, C., Kunz, A., Spang, R., Grooß, J.-U., and Riese, M.: Horizontal water vapor transport in the lower stratosphere from subtropics to high latitudes during boreal summer, J. Geophys. Res., 118, 8111–8127, doi:10.1002/jgrd.50636, 2013.

Pommrich, R., Müller, R., Grooß, J.-U., Konopka, P., Günther, G., Pumphrey, H.-C., Viciani, S., D'Amato, F., and Riese, M.: Carbon monoxide as a tracer for tropical troposphere to stratosphere transport in the Chemical Lagrangian Model of the Stratosphere (CLaMS), Geosci. Model Dev. Discuss., 4, 1185–1211, doi:10.5194/gmdd-4-1185-2011, 2011.

Riese, M., Ploeger, F., Rap, A., Vogel, B., Konopka, P., Dameris, M., and Forster, P.: Impact of uncertainties in atmospheric mixing on simulated UTLS composition and related radiative effects, J. Geophys. Res., 117, D16305, doi:10.1029/2012JD017751, 2012.

Sander, S. P., Friedl, R. R., Barker, J. R., Golden, D. M., Kurylo, M. J., Wine, P. H., Abbatt, J. P. D., Burkholder, J. B., Kolb, C. E., Moortgat, G. K., Huie, R. E., and Orkin, V. L.: Chemical kinetics and photochemical data for use in atmospheric studies, JPL Publication 10-6, 2011.

Scarchilli, C., Adriani, A., Cairo, F., Donfrancesco, G. D., Buontempo, C., Snels, M., Moriconi, M. L., Deshler, T., Larsen, N., Luo, B. P., Mauersberger, K., Ovarlez, J., Rosen, J., and Schreiner, J.: Determination of polar stratospheric cloud particle refractive indices by use of in situ optical measurements and T-matrix calculations, Appl. Optics, 44, 3302–3311, doi:10.1364/AO.44.003302, 2005.

Shi, Q., Jayne, J. T., Kolb, C. E., Worsnop, D. R., and Davidovits, P.: Kinetic model for reaction of $ClONO_2$ with H_2O and HCl and HOCl with HCl in sulfuric acid solutions, J. Geophys. Res., 106, 24259–24274, doi:10.1029/2000JD000181, 2001.

Solomon, S.: Stratospheric ozone depletion: A review of concepts and history, Rev. Geophys., 37, 275–316, doi:10.1029/1999RG900008, 1999.

Sumińska-Ebersoldt, O., Lehmann, R., Wegner, T., Grooß, J.-U., Hösen, E., Weigel, R., Frey, W., Griessbach, S., Mitev, V., Emde, C., Volk, C. M., Borrmann, S., Rex, M., Stroh, F., and von Hobe, M.: ClOOCl photolysis at high solar zenith angles: analysis of the RECONCILE self-match flight, Atmos. Chem. Phys., 12, 1353–1365, doi:10.5194/acp-12-1353-2012, 2012.

Toon, O. B., Tolbert, M. A., Koehler, B. G., Middlebrook, A. M., and Jordan, J.: Infrared optical constants of H_2O ice, amorphous nitric acid solutions, and nitric acid hydrates, J. Geophys. Res., 99, 25631–25654, doi:10.1029/94JD02388, 1994.

Voigt, C., Larsen, N., Deshler, T., Kröger, C., Schreiner, J., Mauersberger, K., Luo, B., Adriani, A., Cairo, F., Di Donfrancesco, G., Ovarlez, J., Ovarlez, H., Dörnbrack, A., Knudsen, B., and Rosen, J.: In situ mountain-wave polar stratospheric cloud measurements: Implications for nitric acid trihydrate formation, J. Geophys. Res., 108, 8331, doi:10.1029/2001JD001185, 2003.

Voigt, C., Schlager, H., Luo, B. P., Dörnbrack, A., Roiger, A., Stock, P., Curtius, J., Vössing, H., Borrmann, S., Davies, S., Konopka, P., Schiller, C., Shur, G., and Peter, T.: Nitric Acid Trihydrate (NAT) formation at low NAT supersaturation in Polar Stratospheric Clouds (PSCs), Atmos. Chem. Phys., 5, 1371–1380, doi:10.5194/acp-5-1371-2005, 2005.

Vömel, H., David, D. E., and Smith, K.: Accuracy of tropospheric and stratospheric water vapor measurements by the cryogenic frost point hygrometer: Instrumental details and observations, J. Geophys. Res., 112, D08305, doi:10.1029/2006JD007224, 2007.

von Clarmann, T., Höpfner, M., Kellmann, S., Linden, A., Chauhan, S., Funke, B., Grabowski, U., Glatthor, N., Kiefer, M., Schieferdecker, T., Stiller, G. P., and Versick, S.: Retrieval of temperature, H_2O, O_3, HNO_3, CH_4, N_2O, $ClONO_2$ and ClO from MIPAS reduced resolution nominal mode limb emission measurements, Atmos. Meas. Tech., 2, 159–175, doi:10.5194/amt-2-159-2009, 2009.

von Hobe, M., Grooß, J.-U., Günther, G., Konopka, P., Gensch, I., Krämer, M., Spelten, N., Afchine, A., Schiller, C., Ulanovsky, A., Sitnikov, N., Shur, G., Yushkov, V., Ravegnani, F., Cairo, F., Roiger, A., Voigt, C., Schlager, H., Weigel, R., Frey, W., Borrmann, S., Müller, R., and Stroh, F.: Evidence for heterogeneous chlorine activation in the tropical UTLS, Atmos. Chem. Phys., 11, 241–256, doi:10.5194/acp-11-241-2011, 2011.

von Hobe, M., Bekki, S., Borrmann, S., Cairo, F., D'Amato, F., Di Donfrancesco, G., Dörnbrack, A., Ebersoldt, A., Ebert, M., Emde, C., Engel, I., Ern, M., Frey, W., Genco, S., Griessbach, S., Grooß, J.-U., Gulde, T., Günther, G., Hösen, E., Hoffmann, L., Homonnai, V., Hoyle, C. R., Isaksen, I. S. A., Jackson, D. R., Jánosi, I. M., Jones, R. L., Kandler, K., Kalicinsky, C., Keil, A., Khaykin, S. M., Khosrawi, F., Kivi, R., Kuttippurath, J., Laube, J. C., Lefèvre, F., Lehmann, R., Ludmann, S., Luo, B. P., Marchand, M., Meyer, J., Mitev, V., Molleker, S., Müller, R., Oelhaf, H., Olschewski, F., Orsolini, Y., Peter, T., Pfeilsticker, K., Piesch, C., Pitts, M. C., Poole, L. R., Pope, F. D., Ravegnani, F., Rex, M., Riese, M., Röckmann, T., Rognerud, B., Roiger, A., Rolf, C., Santee, M. L., Scheibe, M., Schiller, C., Schlager, H., Siciliani de Cumis, M., Sitnikov, N., Søvde, O. A., Spang, R., Spelten, N., Stordal, F., Sumin'ska-Ebersoldt, O., Ulanovski, A., Ungermann, J., Viciani, S., Volk, C. M., vom Scheidt, M., von der Gathen, P., Walker, K., Wegner, T., Weigel, R., Weinbruch, S., Wetzel, G., Wienhold, F. G., Wohltmann, I., Woiwode, W., Young, I. A. K., Yushkov, V., Zobrist, B., and Stroh, F.: Reconciliation of essential process parameters for an enhanced predictability of Arctic stratospheric ozone loss and its climate interactions (RECONCILE): activities and results, Atmos. Chem. Phys., 13, 9233–9268, doi:10.5194/acp-13-9233-2013, 2013.

Wegner, T., Grooß, J.-U., von Hobe, M., Stroh, F., Sumin'ska-Ebersoldt, O., Volk, C. M., Hösen, E., Mitev, V., Shur, G., and Müller, R.: Heterogeneous chlorine activation on stratospheric aerosols and clouds in the Arctic polar vortex, Atmos. Chem. Phys., 12, 11095–11106, doi:10.5194/acp-12-11095-2012, 2012.

Wohltmann, I., Wegner, T., Müller, R., Lehmann, R., Rex, M., Manney, G. L., Santee, M. L., Bernath, P., Sumin'ska-Ebersoldt, O., Stroh, F., von Hobe, M., Volk, C. M., Hösen, E., Ravegnani, F., Ulanovsky, A., and Yushkov, V.: Uncertainties in modelling heterogeneous chemistry and Arctic ozone depletion in the winter 2009/2010, Atmos. Chem. Phys., 13, 3909–3929, doi:10.5194/acp-13-3909-2013, 2013.

Woiwode, W.: Qualification of the airborne FTIR spectrometer MIPAS-STR and study on denitrification and chlorine deactivation in Arctic winter 2009/10, Dissertation, Karlsruhe Insitute for Technology, Faculty of Chemistry and Biosciences, Karlsruhe, Germany, 2013.